ENGINEERING

Twin-free, directly synthesized MFI nanosheets with improved thickness uniformity and their use in membrane fabrication

Donghun Kim[1], Supriya Ghosh[2], Nusnin Akter[3], Andrea Kraetz[4], Xuekui Duan[2], Gyeongseok Gwak[1], Neel Rangnekar[5], J. R. Johnson[5], Katabathini Narasimharao[6], Maqsood Ahmad Malik[6], Shaeel Al-Thabaiti[6], Benjamin McCool[5], J. Anibal Boscoboinik[3], K. Andre Mkhoyan[2], Michael Tsapatsis[4,7]*

Zeolite nanosheets can be used for the fabrication of low-defect-density, thin, and oriented zeolite separation membranes. However, methods for manipulating their morphology are limited, hindering progress toward improved performance. We report the direct synthesis (i.e., without using exfoliation, etching, or other top-down processing) of thin, flat MFI nanosheets and demonstrate their use as high-performance membranes for xylene isomer separations. Our MFI nanosheets were synthesized using nanosheet fragments as seeds instead of the previously used MFI nanoparticles. The obtained MFI nanosheets exhibit improved thickness uniformity and are free of rotational and MEL intergrowths as shown by transmission electron microscopy (TEM) imaging. The nanosheets can form well-packed nanosheet coatings. Upon gel-free secondary growth, the obtained zeolite MFI membranes show high separation performance for xylene isomers at elevated temperature (e.g., *p*-xylene flux up to 1.5×10^{-3} mol m^{-2} s^{-1} and *p*-/*o*-xylene separation factor of ~600 at 250°C).

INTRODUCTION

Zeolite membranes already find uses in solvent dehydration and meet requirements for commercialization of certain improved energy efficiency separation processes, like the separation of carbon dioxide from methane (*1*–*6*). For more difficult separations (like hydrocarbon isomer and olefin/paraffin separations) (*7*–*10*) and for challenging operation environments (e.g., as encountered in membrane reactors) (*11*–*14*), compositional and microstructural optimization is required for improving separation performance (*15*–*24*). For example, separation of xylene isomers in a membrane reactor configuration requires high flux and high selectivity at high pressure and temperature, which necessitates thin and preferentially oriented membranes when the membranes are made by the MFI-type zeolite (*4*, *15*, *16*, *18*). However, the simultaneous control of framework structure and composition, crystal orientation, grain size, and intergrowth remains a major challenge.

When preferred orientation, small membrane thickness, and specific microstructural characteristics are desirable, zeolite nanosheets are highly attractive building blocks, as their large aspect ratio and few-nanometer thickness allow the formation of oriented, low-defect-density, and thin membranes. Zeolite nanosheets were first prepared by exfoliation of multilamellar zeolites (*25*–*29*), later by direct synthesis (*30*), and, more recently, by anisotropic etching of zeolite crystals (*31*). Exfoliation and etching are both top-down methods, which may compromise the structural integrity of nanosheets or limit the attainable thickness. For example, although exfoliated MFI nanosheets that exhibit uniform thickness of 3 nm (1.5 unit cells) can be prepared, their in-plane dimensions are limited to well below 1 μm, because of fragmentation. MFI nanosheets made by etching can be extended to ca. 7.5 μm laterally, but they are relatively thick (e.g., not thinner than 25 nm). Direct synthesis methods offer several advantages, such as potential for higher product yields and larger lateral dimensions and aspect ratios, while offering a synthesis procedure that is compatible with established zeolite synthesis methods.

The first direct synthesis of zeolite MFI nanosheets (*30*) was developed on the basis of the seeded hydrothermal growth using a diammonium-cation [*bis*-1,5(tripropyl ammonium) pentamethylene diiodide, which we call dC5] structure directing agent. MFI nanocrystals were used as seeds to enable the synthesis of individual (nonintergrown), separate (nonaggregated) nanosheets. The direct growth of nanosheets proceeds through the occurrence of a single rotational intergrowth after the seed crystals attain a certain size and shape. This approach provides high–aspect ratio, thin nanosheets. However, the nanosheets contain the seed nanocrystals embedded at their center, resulting in a complex morphology deviating from that of an ideal two-dimensional shape. Although ultraselective para-xylene MFI membranes have been prepared using these directly synthesized MFI nanosheets, it is desirable to attempt direct synthesis of MFI nanosheets with more uniform thickness and absent rotational intergrowths and to explore the permeation properties of the corresponding membranes. Here, we report a modified direct synthesis method for novel zeolite MFI nanosheets exhibiting improved thickness and structure uniformity compared to previously reported ones, and the resulting xylene isomer separation performance of membranes fabricated using these nanosheets.

[1]School of Chemical Engineering, Chonnam National University, Gwangju 61186, Republic of Korea. [2]Department of Chemical Engineering and Materials Science, University of Minnesota, Minneapolis, MN 55455, USA. [3]Center for Functional Nanomaterials, Brookhaven National Laboratory, Upton, NY 11973, USA. [4]Department of Chemical and Biomolecular Engineering and Institute for NanoBiotechnology, Whiting School of Engineering, Johns Hopkins University, Baltimore, MD 21218, USA. [5]Separations and Process Chemistry, Corporate Strategic Research, ExxonMobil Research and Engineering, Annandale, NJ 08801, USA. [6]Department of Chemistry, Faculty of Science, King Abdulaziz University, Jeddah 21589, Saudi Arabia. [7]Applied Physics Laboratory, Johns Hopkins University, Laurel, MD 20723, USA.
*Corresponding author. Email: tsapatsis@jhu.edu

RESULTS

Preparation of zeolite MFI nanosheet fragments

Seeded growth with dC5 can produce rhombus-shaped MFI nanosheets with ca. 2-μm lateral dimensions and predominantly 5-nm thickness, which can be used for the fabrication of high-performance zeolite MFI membranes (*30*). Under certain synthetic conditions (composition, temperature, and time), a single rotational intergrowth per nanocrystalline seed triggers the formation of nanosheets surrounding the nanocrystal seeds (Fig. 1A). However, these rhombus-shaped nanosheets have morphologies distinct from typical nanosheets because they contain ca. 100-nm nanocrystals at their center, which originate from the ca. 20-nm seeds used for nanosheet synthesis. The nanocrystal seeds play a key role in achieving individual separated nanosheets by suppressing the occurrence of

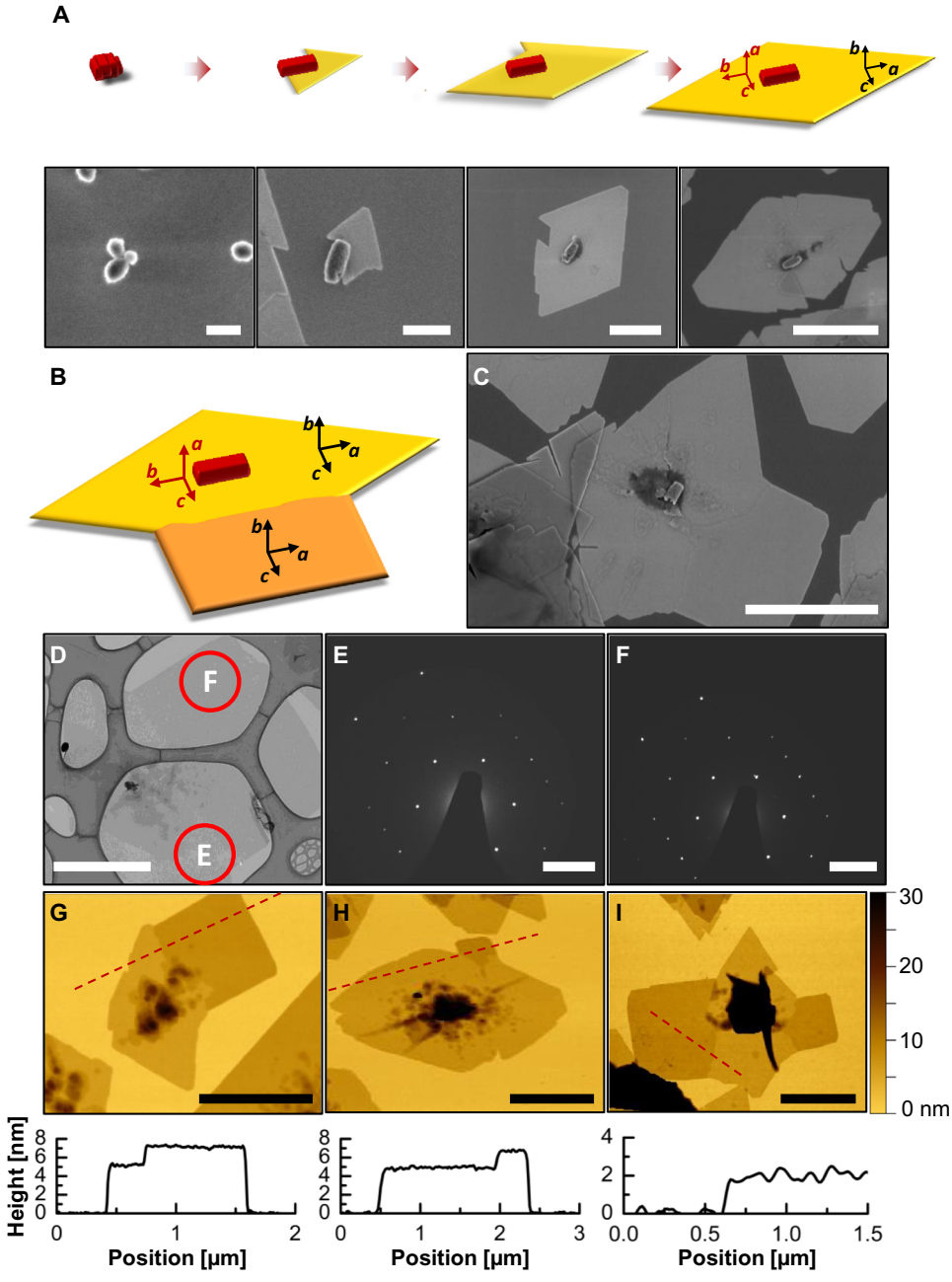

Fig. 1. Rectangular outgrowth of zeolite MFI nanosheet. (**A**) Schematic and the corresponding SEM images of the sequence leading to MFI rhombus-shaped nanosheets, as reported in (*30*). (**B**) Schematic of the rectangular outgrowth and (**C**) corresponding representative SEM image. (**D**) Low-magnification TEM image and (**E** and **F**) selected area diffraction patterns of nanocrystal-seeded zeolite MFI nanosheet. An overlaid outline of the nanosheet and outgrowth is shown in fig. S2. The rhombus nanosheet and rectangular outgrowth have identical crystal orientations, as confirmed by their corresponding SAED shown in (E) and (F), respectively. (**G** to **I**) AFM images of nanocrystal-seeded zeolite MFI nanosheets with rectangular outgrowths and corresponding height profiles extracted from the dotted lines showing 2-nm step at rhombus/outgrowth boundary. Scale bars from left to right in (A), 200 nm, 200 nm, 500 nm, and 1 μm. Scale bars, 1 μm (C), 1 μm (D), 1 nm^{-1} (E and F), 1 μm (G to I).

multiple rotational intergrowths (*32*). This unconventional morphology (i.e., with the presence of a nanocrystal at the center of each nanosheet) may affect the membrane performance by hindering the close-packing of nanosheets when they are deposited on substrates. Moreover, because the nanosheets and seeds are 90° rotated to each other around their common *c* axis, there is always an *a*-out-of-plane–oriented fraction in these predominantly *b*-oriented membranes, which, along with the associated twin boundaries, may also affect membrane performance. To explore the effect of well-packed nanosheet coatings and the absence of *a*-out-of-plane grains on the membrane performance, we have sought the preparation of flatter, more uniformly structured zeolite MFI nanosheets (i.e., without the single rotational intergrowth present in the nanocrystal-seed-grown nanosheets). The strategy reported here is based on using seeds with nanosheet morphology, thus eliminating the formation of the rotational intergrowth.

First, we describe some early observations that led to the development of the new strategy. During the later stages of synthesis of rhombus-shaped nanosheets from nanocrystal seeds, we have observed the formation of rectangular-shaped outgrowths attached to rhombus nanosheets, as shown in Fig. 1 (B and C). In more detail, following the previously described seeded-growth process that forms {*h0l*} faceted rhombus-shaped nanosheets (Fig. 1A) (*30*), flat rectangular outgrowths begin to emerge expressing {*h*00} and {00*l*} facets (Fig. 1, B and C), which eventually can surround the original rhombus nanosheet (see the particle marked as 3 in fig. S1A). The fraction of nanosheets with outgrowths is small at 140°C but increases with increasing synthesis temperature (fig. S1, B and C). Transmission electron microscopy (TEM) imaging combined with selected area electron diffraction (SAED), shown in Fig. 1 (D to F), revealed that the rectangular outgrowths (SAED shown in Fig. 1F) have the same crystal orientation as the rhombus-shaped nanosheets (SAED shown in Fig. 1E), implying their epitaxial growth. This also confirms that the outgrowths expose the {*h*00} and {00 *l*} facets, while the rhombus-shaped nanosheets expose the {*h0l*} facets, as shown in the cartoon of Fig. 1B. Figure 1G shows atomic force microscopy (AFM) height images of MFI rhombus-shaped nanosheets with rectangular outgrowths. The images and the traces marked as 1 and 2 confirm that the thickness of the rhombus-shaped nanosheets is ca. 5 nm [as reported earlier (*30*)], while the thickness increases abruptly to 7 nm on the rectangular outgrowth. The 2-nm step size at the boundary of the rhombus-shaped nanosheet with the rectangular outgrowth corresponds to 1 unit cell of MFI along its *b* axis (i.e., the thickness of two pentasil chains). We have previously observed that during the formation of the rhombus-shaped nanosheets, thickness originated at 1 nm (0.5 unit cell; one pentasil chain thick), progressed to 3 nm, and then stabilized at a predominant thickness of 5 nm during their early growth stages (*30*). The drastic change of faceting between rhombus nanosheet and rectangular outgrowth is correlated with the increased thickness by 1 unit cell to 7 nm.

Although fundamental understanding of these phenomena remains elusive, these observations suggest that rectangular nanosheets can emerge as outgrowths on the facets of rhombus nanosheets with minimal (1 unit cell) thickening. Therefore, we hypothesized that if fragments of rhombus-shaped nanosheets were used as seeds, they could trigger the formation of nanosheet outgrowths with improved thickness and structural uniformity (i.e., without the presence of the rotationally intergrown seed at the nanosheet center).

Figure 2A depicts the synthesis method of MFI nanosheets with improved thickness uniformity based on the secondary growth of nanosheet fragments. First, rhombus-shaped MFI nanosheets synthesized using MFI nanocrystal seeds were fractured and purified to obtain nanocrystal seed–free nanosheet fragments. Upon an additional growth with a dC5–silica sol, these nanosheet fragments serve as seeds and grow to yield large flat MFI nanosheets without rotationally intergrown nanocrystals embedded at their center.

In more detail, the synthesis procedure starts with zeolite MFI nanosheets made by using nanocrystal seeds, as reported previously (*30*), but with an important modification; instead of the ca. 20-nm nanocrystals, larger nanocrystals with size of ca. 100 nm (Fig. 2B) were used to facilitate the subsequent separation step, which aims to remove the seed nanocrystals from the fractured nanosheets and obtain seed-free nanosheet fragments. The nanosheets formed by the hydrothermal treatment of 100-nm nanocrystal seeds with a dC5–silica sol at 155°C (see Materials and Methods for details and compositions) are shown in Fig. 2C. These nanosheets were fractured by using a horn sonicator (Fig. 2D). Centrifugation was then performed to selectively collect a fraction of the fragmented nanosheets that is free of seed nanocrystals and large aggregates as shown in Fig. 2E.

Synthesis of zeolite MFI nanosheets with improved thickness and structure uniformity

The acquired nanocrystal-seed-free MFI nanosheet fragments were then used as a new type of seed to grow MFI nanosheets without rotational intergrowths and yield individual, separated nanosheets. The nanosheet fragments were added to a dC5–silica sol and subjected to a hydrothermal treatment at 155°C. At certain conditions (see Materials and Methods), the fragments maintain their nanosheet morphology and grow into larger nanosheets, as shown in Fig. 3 (A to C) [scanning electron microscopy (SEM) images] and Fig. 3D (TEM image). The majority of nanosheets are rectangular, with only a small fraction of smaller nanosheets having a rhombus shape (indicated by arrows in Fig. 3A). High-resolution TEM (HRTEM) imaging (Fig. 3E) and SAED (Fig. 3F) confirm that the thin dimension of the novel nanosheets is along the *b* axis, while the longer and shorter lateral dimensions are along the *c* and *a* axes, respectively. The majority of novel nanosheets exhibit rectangular shapes with {*h*00} and {00*l*} facets and linear dimensions of ca. 3 and 2 μm along their longer *c* and shorter *a* axes, respectively (Fig. 3G). AFM measurements (Fig. 3, H and I, and fig. S3) show that the thickness of the novel rectangular nanosheets in their thinner portion is 7.2 ± 0.2 nm, corresponding to a thickness of 3.5 MFI unit cells. This is 1 unit cell thicker than the nanocrystal-seeded rhombus nanosheets reported previously (ca. 5 nm) (*30*) and corresponds to the thickness of the rectangular outgrowths presented in Fig. 1.

The novel nanosheets (i.e., the nanosheets made using nanosheet fragments as seeds) exhibit enhanced thickness uniformity compared with nanocrystal-seeded nanosheets because of the elimination of the central rotationally intergrown seed. Yet, they still experience thickening because of ad-layer formation, which unavoidably happens during secondary growth. Because the central part of the nanosheet is growing for a longer period, more layers can nucleate there, and thickening is more pronounced in the center while it is absent from the freshly grown periphery of the nanosheets that are ca. 7 nm thick. For example, AFM height profiles of the

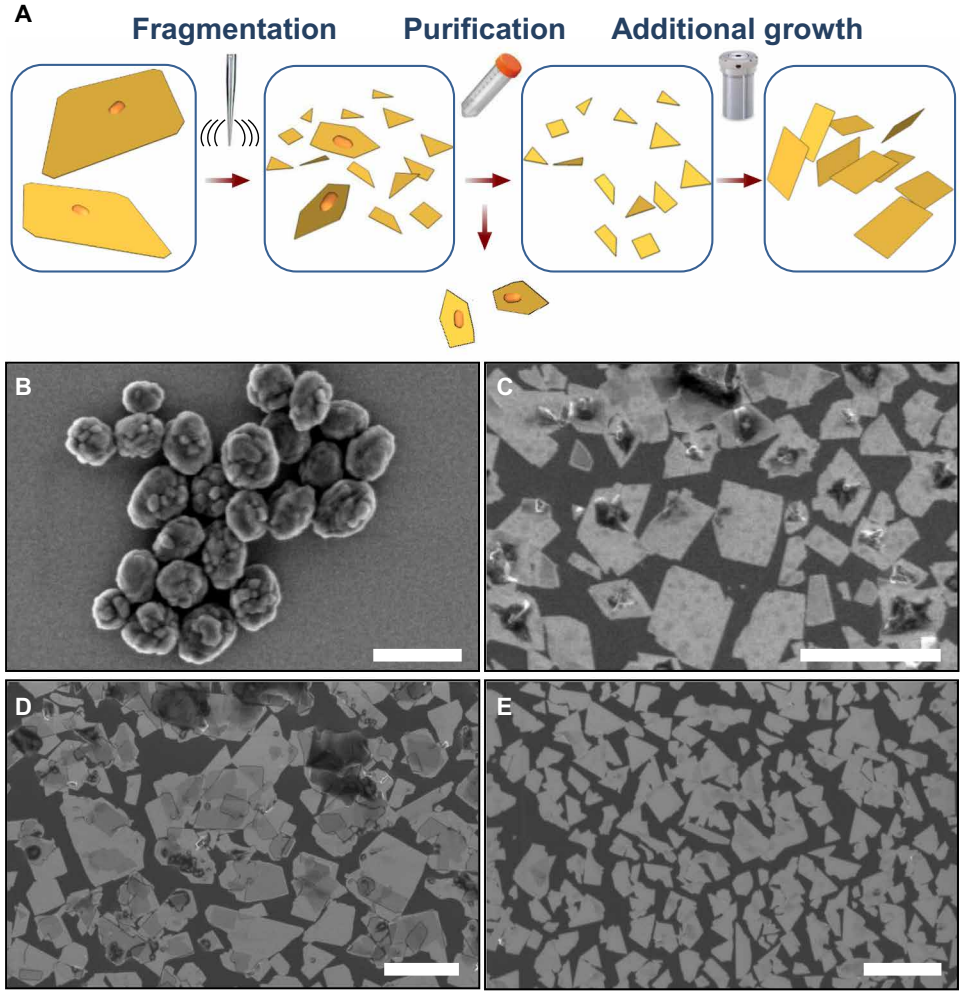

Fig. 2. Preparation of zeolite MFI nanosheet fragments. (**A**) Schematic illustration of the preparation of flat zeolite MFI nanosheets. SEM images for (**B**) MFI nanocrystal seeds, (**C**) MFI nanosheets obtained using the seeds shown in (B), **(D)** fractured MFI nanosheets obtained by sonication of nanosheets shown in (C), and (**E**) MFI nanosheet fragments acquired after purification using centrifugation. The zeolite MFI nanocrystals shown in (B) were hydrothermally treated with a dC5–silica sol at 155°C to yield the MFI nanosheets shown in (C). The nanosheets in (C) were then fractured with a horn sonicator to yield the material shown in (D). After the purification with centrifugation, the nanosheet fragments shown in (E) were obtained. Details are described in Materials and Methods. Scale bars, 200 nm (B), 5 μm (C), 2 μm (D and E).

nanosheet-seeded rectangular nanosheets (Fig. 3I, bottom, and fig. S3) revealed the maximum height is 40 ± 14 nm, which is smaller than those of the nanocrystal-seeded rhombus nanosheets (108 ± 24 nm) reported in (*30*), but considerably thicker than the fragmented nanosheet seeds and the 7-nm-thin periphery of the nanosheets. Because nucleation of additional layers increases as the lateral dimensions increase (*33*), nanosheets with smaller lateral dimensions experience less ad-layer formation and consequently exhibit greater thickness uniformity, as shown in fig. S4.

The novel nanosheet-seeded nanosheets also exhibit improved structural uniformity compared with the nanocrystal-seeded nanosheets. The formation of the previously reported nanocrystal-seeded nanosheets is triggered by a rotational intergrowth. Thereby, the crystallographic orientation of the seed nanocrystal is 90° rotated with respect to the nanosheet along its common *c* axis (see Fig. 1B) (*30*). Upon gel-free growth for membrane fabrication from these nanocrystal-seeded nanosheets, an *a*-out-of-plane–oriented portion is present within the preferentially *b*-out-of-plane–oriented zeolite MFI membranes (*30*). In contrast, a rotational intergrowth is not encountered for the secondary growth of nanosheet fragments, and the obtained nanosheets are all uniformly oriented (fig. S5).

The occurrence of rotational intergrowths in MFI has been associated with the presence of MEL intergrowths (*34*), and one-dimensional MEL intergrowths have been detected in MFI nanosheets prepared by exfoliation of multilamellar MFI (*35*). The absence of a rotational intergrowth in the synthesis approach reported here implies that the novel nanosheet-seeded rectangular MFI nanosheets exhibit a high MFI–phase purity. By using a combination of TEM imaging and SAED, we have investigated multiple nanosheets to identify any structural irregularities (some examples are shown in fig. S6). All but one of the 46 SAED patterns collected revealed the typical [010] zone axis (*b*-oriented) pattern with no elongation observed in any of the diffraction spots, establishing pure MFI frameworks. Only one of the 46 nanosheets studied showed slight elongation in the (102) and (104) diffraction spots in a small region of the nanosheet, which could be due to the presence of trace MEL (see fig. S6, A and B).

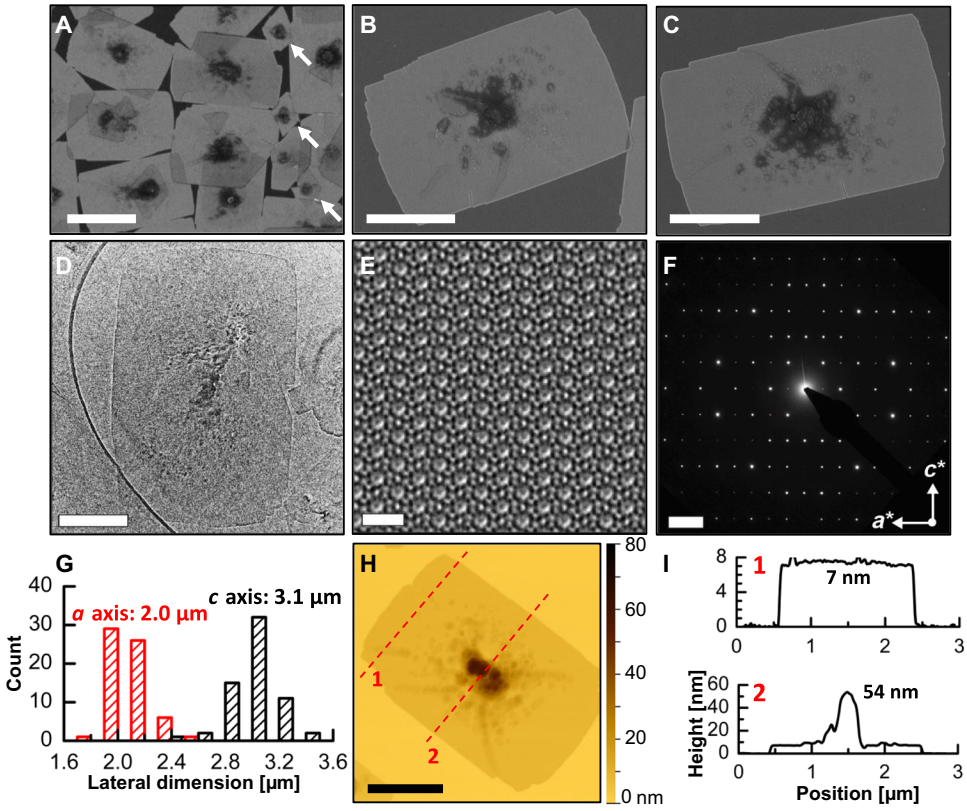

Fig. 3. Characterization of novel zeolite MFI nanosheets. (**A** to **C**) SEM images of the novel (nanosheet-seeded) zeolite MFI nanosheets synthesized from the secondary growth of nanosheet fragments. (**D**) A low-magnification TEM image, (**E**) Wiener-filtered HR-TEM image, and (**F**) SAED pattern of the novel zeolite MFI nanosheets. (**G**) Lateral size distributions (along the *a* and *c* axes) and (**H**) AFM height image of a typical novel zeolite MFI nanosheet. (**I**) Height profiles extracted from the dotted lines in (H). The nanosheets exhibit a rectangular shape with a small fraction having a rhombus shape [indicated by arrows in (A)]. Scale bars, 2 μm (A), 1 μm (B to D), 2 nm (E), 1 nm^{-1} (F), 1 μm (H).

Similar to the previous nanosheets, the novel nanosheets are also able to form a monolayer at the air-water interface, which can then be transferred to a substrate using the floating particle coating method that we have introduced earlier (Fig. 4A) (*36*). The method uses the geometry of a conical-shape trough to increase the density of nanosheets in the monolayer as it is transferred onto a substrate by lowering the water level. Figure 4B shows an SEM image of the acquired nanosheet coating on the Si wafer, which exhibits a dense and uniform nanosheet monolayer consisting of mostly rectangular nanosheets with a minor fraction of smaller rhombus nanosheets. The structure of the novel MFI nanosheets and the orientation of the coating were examined by using in-plane x-ray diffraction (XRD) measurements that provide the structural information regarding the lattice planes perpendicular to the surface. Figure 4C shows an in-plane XRD pattern of a novel MFI nanosheet monolayer (uncalcined), compared to that of a monolayer of nanosheets (uncalcined) prepared by top-down exfoliation (based on melt blending) of multilamellar MFI, and a simulated pattern of conventional MFI crystals (uncalcined). The in-plane XRD pattern of the novel MFI nanosheet monolayer exhibits only the {*h0l*} reflections of conventional MFI. This confirms not only the high-phase purity of the nanosheets but also the *b*-out-of-plane orientation of the monolayers, as the in-plane XRD only probes the lattice planes that are normal to the surface of the substrate. Compared to the top-down exfoliated nanosheet monolayer that is also highly *b*-out-of-plane oriented and exhibits only {*h0l*} reflections, the novel MFI nanosheet monolayer shows less XRD peak broadening (i.e., reduced full width at half maximum), which can be attributed to the larger lateral dimension (2 ~ 3 μm versus 200 ~ 300 nm) and the absence of MEL intergrowths. More specifically, it has been shown that high frequency of single- or near-single unit-cell one-dimensional MEL intergrowths is present in exfoliated nanosheets (*35*). These intergrowths introduce disorder in lattice spacing, not only by their presence and different unit-cell dimensions but also by creating strained MFI domains in their vicinity. This indicates that the novel MFI nanosheets have larger sizes of coherently diffracting domains, which can be attributed to the larger lateral dimensions (2 ~ 3 μm versus 200 ~ 300 nm) and the absence of MEL intergrowths.

Before membrane fabrication, we attempted to characterize the molecular sieving ability of the novel nanosheet-seeded nanosheets. Polarization modulation infrared reflection-absorption spectroscopy (PM-IRRAS) was used to assess xylene adsorption. Surface science methods can provide sufficient signals even from few-nanometer-thick materials, which cannot be achieved by conventional characterization methods. In particular, PM-IRRAS is able to eliminate signals from isotropic gases or solutions, based on the surface selection rule (*37*), and therefore selectively detect xylene molecules adsorbed in MFI frameworks (*38*). The nanosheet-seeded MFI nanosheets were coated on an Au(111) crystal and placed in a high-vacuum chamber with BaF_2 windows that allow the passage of

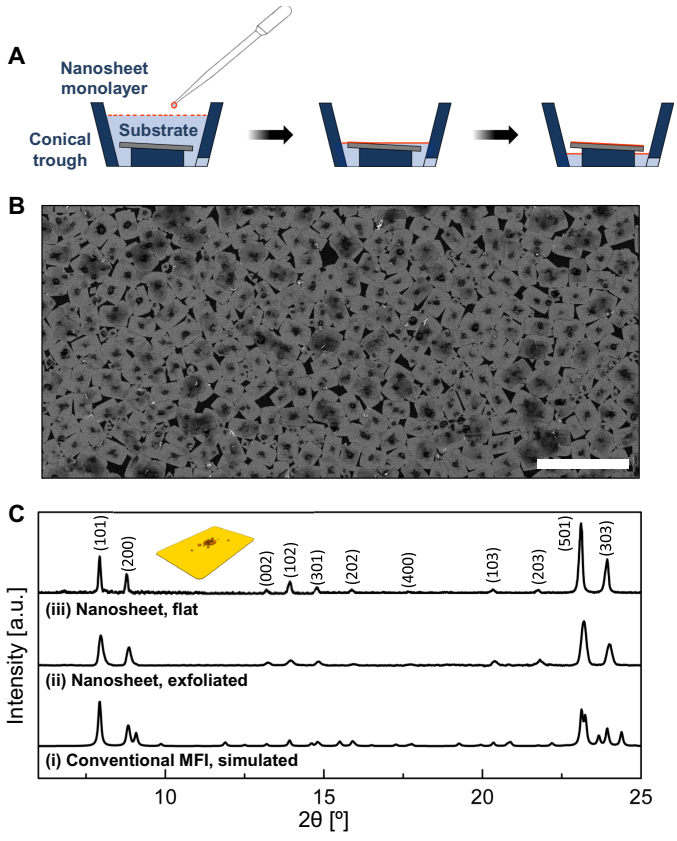

Fig. 4. Zeolite MFI nanosheet monolayer coating. (**A**) Schematic illustration of the monolayer coating procedure of novel (nanosheet-seeded) zeolite MFI nanosheets using the floating particle coating method. (**B**) SEM image of as-synthesized novel zeolite MFI nanosheet monolayer on an Si wafer. (**C**) XRD patterns acquired from (i) a simulation for conventional zeolite MFI (TPA-silicalite-1), (ii) in-plane measurement for a monolayer coating of as-synthesized zeolite MFI nanosheets prepared by top-down processing based on exfoliation of multilamellar MFI using melt-blending, and (iii) in-plane measurement for a monolayer coating of as-synthesized novel zeolite MFI nanosheets. Scale bar, 10 μm (B). a.u., arbitrary unit.

IR light to study phonon vibrations of materials and vibrational modes of adsorbed molecules, under a wide range of pressures and temperatures. Under high vacuum (~2×10^{-4} Pa) and ambient temperature, three phonon modes at 1095, 1176, and 1248 cm^{-1} are obtained, corresponding to MFI framework vibrations (*39*). Exposure to xylene vapor yields additional vibrational modes, which arise from the aromatic ring vibrations of adsorbed xylene molecules. For example, exposure to *p*-xylene[d6] vapor yields an additional vibrational mode at 1438 cm^{-1}, the intensity of which increases with increasing *p*-xylene vapor pressure (fig. S7A). In comparison, an exposure to *o*-xylene results in two bands at 1466 and 1495 cm^{-1} (fig. S7B). When exposed to *p*-/*o*-xylene mixture at a vapor pressure of ~1 kPa, the PM-IRRA spectrum of the nanosheet coating (fig. S7C) exhibits an additional vibrational mode at 1438 cm^{-1}. The selective adsorption of *p*-xylene confirms that the nanosheet-seeded nanosheets exhibit typical MFI *p*-xylene–selective capability.

Fabrication of zeolite MFI membranes from the novel MFI nanosheets

The novel MFI nanosheets were then used to fabricate zeolite MFI membranes. A nanosheet coating was formed on a porous silica support by using the exact floating particle coating procedure as described in (*36*), as shown in Fig. 5A. We followed two approaches to form a well-intergrown membrane: (i) a single gel-free growth of multilayer nanosheet coating (fig. S8) and (ii) multiple gel-free growths of a monolayer nanosheet coating (fig. S9A). For the former approach, multilayer nanosheet coatings (≥3) were prepared by repeating the floating particle coating method and were subjected to the gel-free growth at 180°C (membranes A, B, and C; Fig. 5, C and E). Alternatively, a nanosheet monolayer was subjected to multiple gel-free growths; in this approach, in place of the typically used Stöber silica as the sacrificial silica source (i.e., silica source to grow the deposited nanosheets into a well-intergrown film), mesoporous silica was used instead (fig. S9, B and C). Mesoporous silica is deposited from a homogeneous sol and can fill the gaps between the grains (fig. S9H) more effectively than the Stöber silica nanoparticles, yielding continuous membranes even from a nanosheet monolayer (membrane D; fig. S9, I and J). Detailed synthesis conditions of the four membranes tested are summarized in table S1. A side-by-side comparison of SEM top views of coatings and membranes obtained by the novel and previously reported nanocrystal seed–grown nanosheets is shown in Fig. 5 (A to F). The zeolite MFI membranes acquired from the novel nanosheets consist of well-intergrown, large-size MFI grains. These grains do not have rectangular prism–shaped MFI crystals at their center that are the characteristic feature of the membranes fabricated from nanocrystal-seeded MFI nanosheets (see grains indicated by red arrows in Fig. 5F) (*30*). The cross-sectional SEM image (Fig. 5G) establishes that the thickness of the membrane ranged between 1.0 and 1.8 μm. Although further reduction of the membrane thickness may be possible, especially if the aspect ratio and thickness uniformity of the nanosheets can be increased, we proceed next to evaluate the membrane performance. This performance depends not only on thickness and preferred orientation but also on many additional factors including grain boundary defects, pore blockages among the intergrown crystals, support resistance, and support-zeolite interfaces. In addition, out-of-plane XRD (which probes the lattice planes that are parallel to the surface of the substrate) of the membrane (Fig. 5H) shows a strong (020) reflection. This indicates that the membrane is preferentially *b*-out-of-plane oriented.

Separation performances for xylene isomer binary mixtures

The separation performance of the MFI membranes fabricated from the novel MFI nanosheets was first evaluated for *p*-/*o*-xylene 1:1 mixture at 150°C at a dilute feed condition (a *p*-xylene partial pressure of ~0.3 kPa and an *o*-xylene partial pressure of ~0.3 kPa). At these dilute feed conditions, all zeolite MFI membranes fabricated from multilayer nanosheet coatings (membranes A, B, and C) exhibit very high separation factors (>2000) as well as high permeances in the range of 1.6×10^{-7} to 3.2×10^{-7} mol m^{-2} Pa^{-1} s^{-1} (Table 1) similar to those obtained using the nanocrystal-seeded nanosheets. The zeolite MFI membrane fabricated from a monolayer nanosheet coating (membrane D) also shows a comparable permeance of 3.2×10^{-7} mol m^{-2} Pa^{-1} s^{-1} but a lower separation factor of 843. As the operation temperature increased to 250°C at a comparable feed condition, both permeance and separation factor decreased. For example, as shown in Fig. 6A, membrane D exhibits a permeance of 1.2×10^{-7} mol m^{-2} Pa^{-1} s^{-1} and a separation factor of 341.

The *p*-xylene flux and mixture separation factor of membrane D were further examined with *p*-/*o*-xylene partial pressure in feed in a

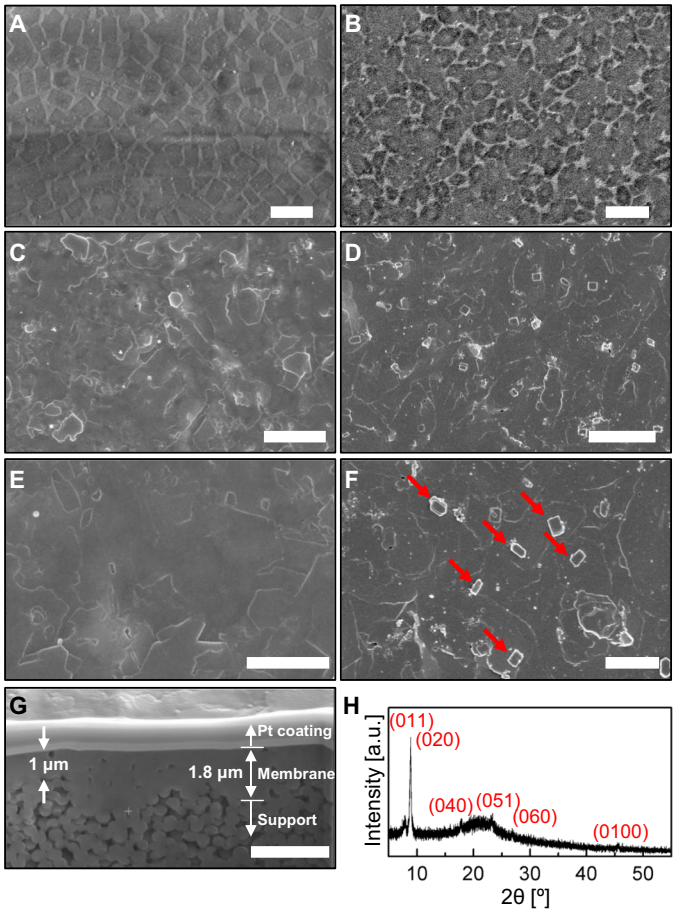

Fig. 5. Zeolite MFI membranes fabricated from nanosheet-seeded nanosheets and nanocrystal-seeded nanosheets. (**A** and **B**) SEM images of zeolite MFI nanosheet coatings on porous silica supports fabricated from (A) novel (nanosheet-seeded) MFI nanosheets and (B) previously reported nanocrystal-seeded MFI nanosheets. (**C** to **F**) SEM images of zeolite MFI membranes fabricated from multilayer coatings of (C and E) novel MFI nanosheets and (D and F) nanocrystal-seeded MFI nanosheets. The red arrows in (F) indicate *a*-oriented grains that are formed from the nanocrystal seeds used for the synthesis of nanosheets. (**G**) Cross-sectional SEM image and (**H**) XRD pattern of a zeolite MFI membrane fabricated from multilayer coating of novel zeolite MFI nanosheets. Scale bars, 5 μm (A and B), 2 μm (C and D), 1 μm (E and F), 2 μm (G).

range between 0.6 and 19.1 kPa, while the isomer molar ratio was maintained to ca. 1 (Fig. 6B). At a dilute feed concentration (~0.3 kPa of *p*-xylene and ~0.3 kPa of *o*-xylene), the *p*-xylene permeance mentioned above corresponds to a flux of only 3.2×10^{-5} mol m^{-2} s^{-1}. As the *p*-xylene concentration in the *p*-/*o*-xylene mixed feed increases, the *p*-xylene flux gradually increased to 6.2×10^{-4} mol m^{-2} s^{-1}, with the increasing feed concentration up to 9.2 kPa of *p*-xylene and 9.9 kPa of *o*-xylene, indicating that the permeance value was not substantially diminished in this range (*p*-xylene permeance of 0.7×10^{-7} mol m^{-2} Pa^{-1}s^{-1}). The separation factor for the *p*-/*o*-xylene mixed feed at this condition, however, shows a reduction to 241.

The permeation properties at elevated temperature and high feed concentration were additionally confirmed for a membrane fabricated from nanosheet multilayers using a single gel-free growth. As shown in Table 1, membrane C exhibits a comparable but slightly higher *p*-xylene flux of 7.4×10^{-4} mol m^{-2} s^{-1} at 250°C with a feed *p*-xylene partial pressure of 7.7 kPa and *o*-xylene partial pressure of 8.3 kPa. In addition, membrane C exhibits a higher separation factor of 610 at this condition. Because ca. 9 kPa of *p*-xylene is the upper limit of the feed concentration for our analysis system when using 1:1 *p*-/*o*-xylene mixture, to assess the permeation properties of the membrane at higher *p*-xylene feed concentration, the feed composition was changed to 9:1 *p*-/*o*-xylene. This yielded an estimated *p*-xylene partial pressure of ~16 kPa in the feed, at which the *p*-xylene permeate flux was increased to 1.5×10^{-3} mol m^{-2} s^{-1}, along with the mixture separation factor of 600.

Figure 6C shows a comparison of *p*-xylene fluxes and *p*-/*o*-xylene separation factors acquired from various separation membranes evaluated for a binary mixture of xylene isomers. Very high separation factors for xylene isomers as well as high *p*-xylene permeances have been reported earlier for a vapor permeation of zeolite MFI membranes (⬟ and ★) (*30*, *36*). Although these separation performances are much higher than vapor permeation of non–crystalline material–based membranes [e.g., carbon molecular sieve (CMS) hollow fibers] (*40*), these were acquired only at dilute feed concentrations, which could not provide practically meaningful fluxes (<1.0×10^{-4} mol m^{-2} s^{-1}). High feed concentrations (47.5 kPa of *p*-xylene and 47.5 kPa of *o*-xylene) have been used for vapor permeation of exfoliated nanosheet–based zeolite MFI membranes, exhibiting increased *p*-xylene fluxes (4.0×10^{-4} to 4.7×10^{-4} mol m^{-2} s^{-1}) but low separation factors of ~60 (*35*). Pervaporation (liquid feed) (◀) using zeolite MFI membranes (*41*) similarly yielded a higher *p*-xylene flux (3.6×10^{-4} mol m^{-2} s^{-1}) and low separation factor (~40). Other molecular sieve materials, MIL-160 (▲) using pervaporation (*42*) and CMS hollow fiber (◁) using a pressure-driven liquid-phase separation (*43*), have provided high *p*-xylene fluxes up to 1.5×10^{-3} mol m^{-2} s^{-1}, although their separation factors are not as high as those obtained with dilute-feed vapor permeation using zeolite MFI membranes. The work reported here (●, ○, and ■) has achieved high *p*-xylene fluxes comparable to other high-flux membranes (CMS hollow fibers and the MIL-160 membranes) while simultaneously exhibiting separation factors (~600), which are more than an order of magnitude higher.

DISCUSSION

We fabricated high-flux and high-selectivity xylene-isomer separation membranes based on novel zeolite MFI nanosheets. Use of nanosheet fragments as seeds allows the preparation of rectangular nanosheets without rotationally intergrown large nanocrystals embedded at the center, yielding improved thickness (predominantly 7 nm) and orientational uniformity. Consequently, the MFI nanosheets with high phase purity could be prepared without the presence of MEL and rotational intergrowth, as established by XRD, TEM-SAED, and STEM. These favorable morphological and structural properties of the novel nanosheets enabled the fabrication of zeolite MFI membranes exhibiting an unprecedented combination of high fluxes and high separation factors for xylene isomers (*p*-xylene permeate flux of 1.5×10^{-3} mol m^{-2} s^{-1} and a separation factor of 600). Although the preparation of nanosheet fragment seeds added more complexity to the material synthesis process, the advantageous properties of the novel zeolite MFI nanosheets have enabled substantially improved productivity.

The yield of novel nanosheets defined as

Table 1. Xylene isomer separation performances of zeolite MFI membranes measured under various operating conditions.

	Temperature (°C)	Partial pressure in feed (kPa)		Permeance (mol·m^{-2} Pa^{-1}·s^{-1})	Flux (mol m^{-2}·s^{-1})	Separation factor
		p-Xylene	*o*-Xylene			
Membrane A*	150	0.34	0.44	2.1×10^{-7}	5.8×10^{-5}	2040
Membrane B*	150	0.29	0.26	1.6×10^{-7}	3.9×10^{-5}	5930
Membrane C*	150	0.35	0.30	3.2×10^{-7}	8.2×10^{-5}	3540
	250	7.7†	8.3†	8.8×10^{-8}‡	7.4×10^{-4}	610
	250	16†	1.7†	1.1×10^{-7}‡	1.5×10^{-3}	600
Membrane D§	150	0.31	0.29	3.2×10^{-7}	7.2×10^{-5}	843
	250	9.2†	9.9†	7.1×10^{-8}‡	6.2×10^{-4}	241‡

*Membranes fabricated from a multilayer nanosheet coating using a single gel-free growth (see table S1 and fig. S8). †Estimated from the vapor pressures of pure *p*-/*o*-xylene at the saturator temperature. ‡Calculated from the estimated partial pressures of *p*-/*o*-xylene in the feed. §Membrane fabricated from a monolayer nanosheet coating using multiple gel-free growths (see table S1 and fig. S9A).

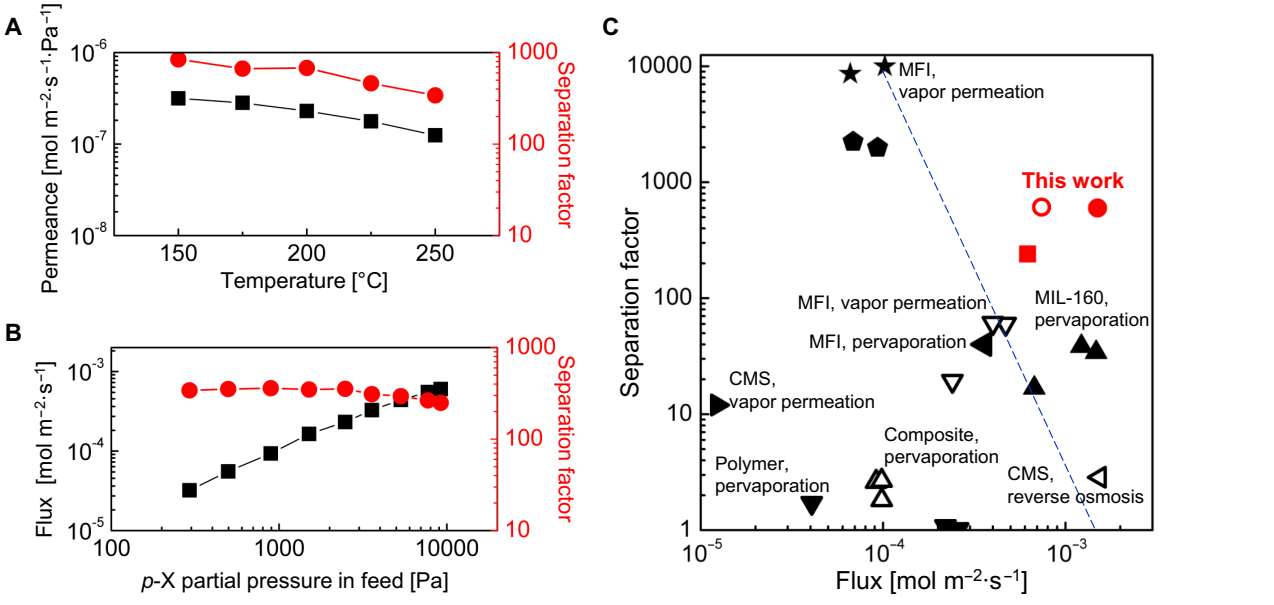

Fig. 6. Separation performance of zeolite MFI membranes for *p*-/*o*-xylene binary mixture. (**A**) *p*-Xylene permeances and separation factors at various operation temperatures and (**B**) *p*-Xylene fluxes and separation factors at various *p*-xylene feed partial pressures (all mixtures with 1:1 *p*- and *o*-xylene) for a zeolite MFI membrane fabricated from a monolayer coating of novel (nanosheet-seeded) zeolite MFI nanosheets [membrane (D) in Table 1]. (**C**) Xylene isomer separation performance at 250°C for the zeolite MFI membranes reported here (○: membrane C, 7.7 kPa of *p*-xylene and 8.3 kPa of *o*-xylene in feed; ●: membrane C, 16 kPa of *p*-xylene and 1.7 kPa of *o*-xylene in feed; and ■: membrane D, 9.2 kPa of *p*-xylene and 9.9 kPa of *o*-xylene in feed) fabricated from the novel zeolite MFI nanosheets compared with other xylene isomer separation membranes from the literature [⬟: (*30*), ▽: (*35*), ★: (*36*), ▶: (*40*), ◀: (*41*), ▲: (*42*), ◁: (*43*) ▼: (*55*), and △: (*56*)]. The dotted line shows the upper boundary for the performances of representative MFI membranes reported earlier.

$$\frac{\text{[Moles of silica in novel nanosheets]}}{\text{[Moles of silica in nanocrystal seeds + Moles of silica used in the two dC5–silica sols]}}$$

is ca. 20 to 30%. To be used as high-quality seed layers, the novel nanosheets have to be purified by centrifugation to remove any aggregates present. During this purification step, a major fraction of high-quality nanosheets is lost by association with the aggregates, arriving to an overall yield defined as

$$\frac{\text{[Moles of silica in novel nanosheets after purification to remove aggregates]}}{\text{[Moles of silica in nanocrystal seeds + Moles of silica used in the two dC5–silica sols]}}$$

of only ca. 1%. All of the purified nanosheets are usable for high-quality coatings, and when using the floating particle method, there are only few wasted nanosheets (i.e., nanosheets that cannot be transferred to the support). We expect that the overall 1% yield could be substantially improved in a scaled-up and optimized synthesis process. However, even this low yield is acceptable in terms of membrane cost. If we consider that 1 g of nanosheets is sufficient to create a 500-nm-thick seed layer per square meter of membrane area, and we assume a cost of nanosheets as high as $10,000/kg (i.e., more than 100 times the cost of conventional all-silica MFI), the cost of nanosheets per membrane area is at most $10/m^2, which

is at least an order of magnitude less than the typical cost of a porous ceramic support. In this respect, the benefit of achieving a 10-fold flux increase (and the corresponding reduction of membrane area requirement) using the novel nanosheets outweighs the increased cost of the seed layer caused by the low yield of novel nanosheets. The achieved flux of 10^{-3} mol/m^2-s is still low for membrane reactor applications, which require that membrane fluxes match the reactor productivity, demanding fluxes as high as 0.1 mol/m^2-s (*44*). Therefore, at least an order of magnitude further increase in flux is required for considering the design of a xylene isomerization membrane reactor.

The high productivity of the membranes reported here is an important breakthrough for the zeolite molecular sieve membranes, as their insufficient productivity, along with the high fabrication cost, has been a major bottleneck in their practical implementation. In earlier studies, zeolite MFI membranes exhibited diminished fluxes at high xylene loading (e.g., high feed concentration) (*45*, *46*). This work demonstrates *p*-xylene permeate fluxes that almost linearly increase with the increasing *p*-xylene concentration in the feed (up to ~16 kPa of *p*-xylene) at 250°C. In future studies, we will attempt to investigate even higher pressures and temperatures aiming to further increase in flux.

MATERIALS AND METHODS

Preparation of zeolite nanosheet fragments

Zeolite nanosheet fragments were prepared from nanocrystal-seeded zeolite MFI nanosheets (*30*). First, the MFI nanocrystal seeds were synthesized with tetrapropylammonium hydroxide (TPAOH); TPAOH–silica sol was prepared by mixing 8.93 g of 1.0 M TPAOH solution, 0.16 g of deionized (DI) water, 0.127 g of sodium hydroxide, and 2.5 g of silicic acid. After overnight stirring under ambient conditions, the entire TPAOH–silica sol was transferred into a 45 ml–volume Teflon-lined stainless-steel autoclave and hydrothermally treated at 115°C for 3 days. The obtained MFI nanocrystal seeds were washed three times with DI water as follows, before the synthesis of MFI nanosheets. One microliter of MFI nanocrystal suspension (~0.16 $g_{nanocrystal}$/$ml_{dispersion}$) was transferred into a microcentrifuge tube and was diluted to 2 ml by adding water, and then, the MFI nanocrystals were collected by centrifugation at 14,500 RCF (relative centrifugal force) for 5 min, followed by decantation. The MFI nanocrystals were redispersed in DI water by using an ultrasonication bath. The washing process using the centrifugation at 14,500 RCF was performed twice more. The acquired nanocrystals were redispersed in 2 ml of DI water, and then, the solid content of nanocrystal suspension was determined by drying and weighing an aliquot of the suspension.

Zeolite MFI nanosheets were synthesized from the nanocrystal seeds based on the seeded growth with dC5. The dC5–silica sol was prepared by mixing 0.5494 g of dC5, 0.3141 of KOH (85%), 41.04 g of DI water, and 4 g of tetraethyl orthosilicate. After overnight hydrolysis under ambient conditions, the dC5–silica sol was filtered with a 0.45-μm GHP syringe filter and mixed with nanocrystal suspension to yield a 20:1 silica ratio. Then, the mixture was transferred into a Teflon-lined stainless-steel autoclave and hydrothermally treated at 155°C for 3 days. Because of the increased nanocrystal size, the autoclaves were shaken every 24 hours to redisperse nanocrystals that may have precipitated.

Acquired MFI nanosheets were then fractured by using a horn sonicator. A 1/4″ probe of a Qsonica Q500 ultrasonic processor was inserted into ~23 ml of nanosheet suspension, and the fracturing was performed at 20% amplitude for 120 s. Each pulse was applied for 5 s with 2-s interval. Then, the remaining aggregates, nanocrystals, and thick center parts of nanosheets were separated out of the suspension using centrifugation at 5000 RCF for 30 s. The nanosheet fragment suspension was collected by gently decanting the supernatant into a new centrifuge tube. The centrifugation and decantation process was repeated four additional times.

Secondary growth of fragments

Zeolite MFI nanosheet fragments were used as seeds to prepare novel (nanosheet-seeded) MFI nanosheets. The dC5–silica sol prepared as described above was mixed with a nanosheet fragment suspension to yield 1.5 weight ratio of a precursor sol to a fragment suspension. Then, the mixed solution was transferred into a Teflon-lined stainless-steel autoclave and hydrothermally treated at 155°C for 3 days.

Fabrication of porous supports

A sintered silica support was fabricated from crushed quartz fiber by using a silicon carbide binder (StarPCS SMP-10, Starfire Systems). Silica powder acquired from quartz wool (4-μm diameter) was well mixed with 600 μl of the 10 volume % (vol %) SMP-10 solution in toluene. The mixture was then pressed into a disk using a stainless steel press die with 22-mm diameter at a force of 4000 kg for 30 s. The pressed disks were dried overnight under ambient conditions and then at 70°C for a day. The pressed disks were then thermally treated at 400°C for 6 hours under N_2 atmosphere, to polymerize the inorganic binder, and then thermally treated at 1100°C for 3 hours under air. The ramp rates were 2°C/min for heating and 4°C/min for cooling.

The surfaces of porous silica supports were sequentially polished with 600-grit and 1200-grit SiC polishing papers. Then, the surfaces of supports were further flattened using 500-nm Stöber silica particles, as described previously (*27*). The top surface of a wet support was manually rubbed with the Stöber silica particles and then thermally treated at 1100°C for 3 hours under air with ramp rates of 2°C/min for heating and 4°C/min for cooling. The rubbing process was typically repeated six to eight times to yield a uniform and flat surface.

The sacrificial silica layers for the secondary growth of zeolite MFI (*47*–*49*) were prepared on top of porous silica supports by using 50-nm Stöber silica nanoparticles or mesoporous silica layers. Fifty-nanometer Stöber silica nanoparticles were deposited on porous silica supports with manual rubbing, followed by a heat treatment at 450°C for 6 hours. Alternatively, mesoporous silica layer (SBA-16) was used as a sacrificial silica layer. First, an epoxy layer was applied on the porous silica supports to block the pores between the 500-nm Stöber silica particles. Epoxy solution (5 weight %) prepared in acetone was spin coated on the porous silica supports with 1000 rpm for 1 min. The polymerization of the epoxy layer was facilitated by heat treatment at 70°C for a day. Then, mesoporous silica thin film was fabricated on top of the epoxy layer. Ethanolic Pluronic F127 silica sol, as reported elsewhere (*50*, *51*), was spin coated on the epoxy-coated silica supports with 2000 rpm and 3000 rpm for 30 s each. The mesoporous silica–coated silica supports were dried under ambient condition for 2 days and treated with water vapor at 70°C for 2 days to strengthen the silica framework and prevent pore closing (*51*). Then, polymeric surfactants and epoxy

layers were removed by calcination at 450°C for 6 hours with ramp rates of 1°C/min for heating and 2°C/min for cooling.

Membrane preparation

Zeolite MFI membranes were fabricated from monolayer or multilayer coatings of novel zeolite MFI nanosheets. First, MFI nanosheets were purified with centrifugation to remove large aggregates. One milliliter of suspension was mixed with 1 ml of DI water and was centrifuged at 1700 RCF for 30 s. Then, 1.25 ml of top suspension was transferred to a new microcentrifuge tube and was diluted with water to 2 ml. Second purification with centrifugation was performed at 5000 RCF for 30 s, and the supernatant was gently transferred to a new microcentrifuge tube. The nanosheets were collected by centrifugation at 10,000 RCF for 1 min. After decantation of supernatant, the cake was redispersed in 2 ml of DI water. The rinsing process at 10,000 RCF was additionally performed three times. The final product was redispersed in 3 ml of DI water containing 5 vol % ethanol.

MFI nanosheets were coated on porous supports to form dense and uniform coatings as seeds. For MFI membranes fabricated from multilayer nanosheet coatings (membranes A, B, and C), an MFI nanosheet monolayer was deposited on a porous silica support coated with a top layer of 50-nm Stöber nanoparticles by repeating the floating particle coating method, using the exact procedure as described in (*36*). The nanosheets were immobilized by a heat treatment at 400°C for 6 hours. An additional nanosheet monolayer coating followed by heat treatment was repeated to achieve dense and uniform nanosheet coating on the porous supports. The number of monolayer coatings for each membrane follows table S1. Nanosheet coatings were then intergrown using gel-free growth (*52*). The gel-free growth condition was slightly varied to optimize the extent of intergrowth. In general, a nanosheet coating on a porous silica support was soaked with the TPAOH solution (0.005 to 0.025 M). Excess solution was removed using Kimwipes from the bottom side of the support. The amounts of impregnated solution were in a range between 0.3 and 0.35 g. Then, the coated porous support was placed in a Teflon-lined stainless-steel autoclave that was heated at 180°C for 1 to 4 days. The membrane was then rinsed with DI water and dried overnight at ambient condition. Detailed gel-free conditions are summarized in table S1.

Alternatively, multiple gel-free growths of a monolayer nanosheet coating were pursued to fabricate an MFI membrane (membrane D). An MFI nanosheet monolayer was deposited on a mesoporous silica–coated silica support and immobilized by a heat treatment at 400°C for 6 hours. For the gel-free growth of the nanosheet coating, 100 μl of 0.025 M TPAOH solution was deposited on the coated porous support by dropping with a micropipette. The coated porous support was then placed in a Teflon-lined stainless-steel autoclave. Additional DI water (100 μl) was inserted at the bottom of the liner, while a Teflon sample holder was used to avoid the direct contact of water with the sample. The gel-free growth was performed at 180°C for 2 days. After calcination at 450°C, additional coating of a mesoporous silica layer, calcination, and gel-free growth were sequentially performed twice under the same condition to acquire a well-intergrown MFI membrane.

Characterization

Morphology of novel MFI nanosheets and MFI membranes was investigated with a Hitachi SU8230 with operation voltage of 0.8 to 1.5 kV. MFI nanosheets on Si wafers were imaged without any conductive metal coating layer, but MFI membranes, before their imaging, were coated with Pt (5 nm) to avoid the buildup of charge. For the cross-sectional SEM images, focused ion beam milling was performed on an FEI Helios G4 UX to make a trench on a membrane (12 μm × 8 μm × 10 μm). The cross section of the membrane was also coated with Pt (5 nm), prior to the imaging. HRTEM imaging and electron diffraction were performed on an FEI Tecnai G2F30 (S)TEM microscope operated at an accelerating voltage of 300 kV. HRTEM images were recorded using a Gatan K2 Summit camera operated in the counting mode where individual frames (3710 × 3838 pixels) of 0.5-s exposure were acquired and drift corrected in Digital Micrograph and summed. High-angle annular dark-field (HAADF)–STEM imaging was performed on an aberration-corrected FEI Titan 60-300 (S)TEM microscope, equipped with an analytical Super-Twin pole piece and CEOS DCOR probe corrector. The microscope was operated at 200 kV with a STEM incident probe convergence angle of 25.5 mrad, HAADF detector collection angles of 55 and 200 mrad, and a probe current of 10 pA.

Height profiles of MFI nanosheets were recorded on a Bruker Nanoscope V Multimode 8 operating in a tapping mode. In-plane XRD patterns were collected with synchrotron x-ray source at beamline 33-BM-C (0.7749 Å) of Advanced Photon Source, Argonne National Laboratory. MFI nanosheets coated on Si wafers were placed almost parallel to the incident beam, and the detector was moved in the plane of the substrate surface. 2θ values of acquired data were converted to those corresponding to Cu Kα radiation. XRD patterns of MFI membranes were recorded by using a Panalytical X'Pert Pro diffractometer with Cu Kα radiation at 45 kV and 40 mA.

PM-IRRAS measurement

Xylene adsorption of MFI nanosheets was investigated with PM-IRRAS. The measurements were performed on a home-built in situ PM-IRRAS instrument equipped with a Bruker Vertex 70 spectrometer and a liquid nitrogen–cooled mercury cadmium telluride (MCT) detector [details were described in (*37*)]. The environmental chamber with IR-transparent windows (BaF_2) allows it to perform the measurements under a wide range of temperature (from ambient temperature to ~1000°C) and pressure (from 2×10^{-8} to 1 atm) conditions.

Au(111) single crystal (diameter of 8 mm) was cleaned with cycles of Ar^+ sputtering, followed by annealing to 800 K. The clean crystal was then coated with MFI nanosheets using the exact floating particle coating procedure as described in (*36*). After the calcination at 400°C, the MFI nanosheets on Au(111) were placed in the environmental chamber. PM-IRRA spectra of MFI nanosheets were recorded under vacuum or xylene vapor at various pressures and ambient temperature. The spectrum was recorded repeatedly until no change was observed to confirm the equilibrium. *p*-xylene with deuterated methyl groups was used to be distinguished from *o*-xylene in the PM-IRRA spectra, which otherwise yields overlapped vibrational modes.

Xylene permeation test

Separation performances of zeolite MFI membranes were evaluated by vapor permeation test with *p*-/*o*-xylene binary mixture. The test was performed in Wicke-Kallenbach mode, in which both of the feed and permeate side pressures were kept at atmospheric pressure. The membrane was calcined prior to the test at 450°C for 6 hours with ramp rates of 1°C/min for heating and 2°C/min for cooling.

The membrane was assembled into a home-built stainless steel module sealed with perfluoroelastomer O-rings (Perlast, Precision Polymer Engineering). The module with the membrane was inserted in the furnace and heated to the target temperature with a ramp rate of 1°C/min. Then, the xylene mixture flowed to the feed side of the module. The He gas flow was controlled at 70 ml/min by a mass-flow controller and passed through a saturator containing the *p*-/*o*-xylene mixture to yield 1:1 ratio of *p*-/*o*-xylene in the feed. The concentration of xylene in the feed was adjusted by the temperature of cooling-/heating-water running through the jacket of the saturator (19° to 95°C). The heating water was not heated higher than 95°C. The permeate was collected using sweep gas (He) at a flow rate of 30 ml/min. The transporting lines for xylene were fully heated using electrical heating tapes to avoid the condensation of xylene vapor.

The concentrations of *p*-/*o*-xylene in the feed and permeate were determined using a gas chromatograph (GC) equipped with a flame ionization detector and a capillary column (DB-WAXetr, Agilent). Methane (10 ml/min) was used as an internal standard. For a low-concentration feed measurement (<5 kPa of *p*-xylene), the permeate compositions were measured after 20 hours at each condition. The permeate compositions for high-concentration feed (>5 kPa of *p*-xylene) were determined after 8 hours at each condition to avoid the unattended heating of a large amount of xylene. At least three measurements were conducted to ensure steady-state permeation.

To avoid condensation of xylene vapors in a GC feed system with xylene partial pressure higher than 6 kPa, the feed composition was not determined by GC. Instead, it was estimated from the saturation vapor pressures calculated from the Antoine equation (*53*, *54*) and apparent Henry's law constants determined from low-saturator-temperature conditions. The permeate concentration in all cases was determined by using GC as described above.

SUPPLEMENTARY MATERIALS

Supplementary material for this article is available at https://science.org/doi/10.1126/sciadv.abm8162

REFERENCES AND NOTES

1. M. Kondo, M. Komori, H. Kita, K. Okamoto, Tubular-type pervaporation module with zeolite NaA membrane. *J. Membr. Sci.* **133**, 133–141 (1997).
2. M. A. Carreon, S. Li, J. L. Falconer, R. D. Noble, Alumina-supported SAPO-34 membranes for CO_2/CH_4 separation. *J. Am. Chem. Soc.* **130**, 5412–5413 (2008).
3. J. Okazaki, H. Hasegawa, N. Chikamatsu, K. Yajima, K. Shimizu, M. Niino, DDR-type zeolite membrane: A novel CO_2 separation technology for enhanced oil recovery. *Sep. Purif. Technol.* **218**, 200–205 (2019).
4. N. Rangnekar, N. Mittal, B. Elyassi, J. Caro, M. Tsapatsis, Zeolite membranes –A review and comparison with MOFs. *Chem. Soc. Rev.* **44**, 7128–7154 (2015).
5. K. Sawamura, T. Furuhata, Y. Sekine, E. Kikuchi, B. Subramanian, M. Matsukata, Zeolite membrane for dehydration of isopropylalcohol–water mixture by vapor permeation. *ACS Appl. Mater. Interfaces* **7**, 13728–13730 (2015).
6. Y. Li, Y. Wang, M. Guo, B. Liu, R. Zhou, Z. Lai, High-performance 7-channel monolith supported SSZ-13 membranes for high-pressure CO_2/CH_4 separations. *J. Membr. Sci.* **629**, 119277 (2021).
7. G. Xomeritakis, Z. Lai, M. Tsapatsis, Separation of xylene isomer vapors with oriented MFI membranes made by seeded growth. *Ind. Eng. Chem. Res.* **40**, 544–552 (2001).
8. M. Arruebo, J. L. Falconer, R. D. Noble, Separation of binary C_5 and C_6 hydrocarbon mixtures through MFI zeolite membranes. *J. Membr. Sci.* **269**, 171–176 (2006).
9. H. H. Funke, M. G. Kovalchick, J. L. Falconer, R. D. Noble, Separation of hydrocarbon isomer vapors with silicalite zeolite membranes. *Ind. Eng. Chem. Res.* **35**, 1575–1582 (1996).
10. P. J. Bereciartua, Á. Cantín, A. Corma, J. L. Jordá, M. Palomino, F. Rey, S. Valencia, E. W. Corcoran, P. Kortunov, P. I. Ravikovitch, A. Burton, C. Yoon, Y. Wang, C. Paur, J. Guzman, A. R. Bishop, G. L. Casty, Control of zeolite framework flexibility and pore topology for separation of ethane and ethylene. *Science* **358**, 1068–1071 (2017).
11. X. Dong, H. Wang, Z. Rui, Y. S. Lin, Tubular dual-layer MFI zeolite membrane reactor for hydrogen production via the WGS reaction: Experimental and modeling studies. *Chem. Eng. J.* **268**, 219–229 (2015).
12. H. Li, C. Qiu, S. Ren, Q. Dong, S. Zhang, F. Zhou, X. Liang, J. Wang, S. Li, M. Yu, Na^+-gated water-conducting nanochannels for boosting CO_2 conversion to liquid fuels. *Science* **367**, 667–671 (2020).
13. S.-J. Kim, Y. Liu, J. S. Moore, R. S. Dixit, J. G. Pendergast, D. Sholl, C. W. Jones, S. Nair, Thin hydrogen-selective SAPO-34 zeolite membranes for enhanced conversion and selectivity in propane dehydrogenation membrane reactors. *Chem. Mater.* **28**, 4397–4402 (2016).
14. W. Yue, Y. Li, W. Wei, J. Jiang, J. Caro, A. Huang, Highly selective CO_2 conversion to methanol in a bifunctional zeolite catalytic membrane reactor. *Angew. Chem. Int. Ed.* **60**, 18289–18294 (2021).
15. J. Hedlund, J. Sterte, M. Anthonis, A. J. Bons, B. Carstensen, N. Corcoran, D. Cox, H. Deckman, W. De Gijnst, P. P. de Moor, F. Lai, J. McHenry, W. Mortier, J. Reinoso, J. Peters, High-flux MFI membranes. *Microporous Mesoporous Mater.* **52**, 179–189 (2002).
16. Z. Lai, G. Bonilla, I. Diaz, J. G. Nery, K. Sujaoti, M. A. Amat, E. Kokkoli, O. Terasaki, R. W. Thompson, M. Tsapatsis, D. G. Vlachos, Microstructural optimization of a zeolite membrane for organic vapor separation. *Science* **300**, 456–460 (2003).
17. J. Choi, H.-K. Jeong, M. A. Snyder, J. A. Stoeger, R. I. Masel, M. Tsapatsis, Grain boundary defect elimination in a zeolite membrane by rapid thermal processing. *Science* **325**, 590–593 (2009).
18. T. C. T. Pham, H. S. Kim, K. B. Yoon, Growth of uniformly oriented silica MFI and BEA zeolite films on substrates. *Science* **334**, 1533–1538 (2011).
19. Y. Peng, H. Lu, Z. Wang, Y. Yan, Microstructural optimization of MFI-type zeolite membranes for ethanol–water separation. *J. Mater. Chem. A* **2**, 16093–16100 (2014).
20. L. Yu, S. Fouladvand, M. Grahn, J. Hedlund, Ultra-thin MFI membranes with different Si/Al ratios for CO_2/CH_4 separation. *Microporous Mesoporous Mater.* **284**, 258–264 (2019).
21. Z. Cao, S. Zeng, Z. Xu, A. Arvanitis, S. Yang, X. Gu, J. Dong, Ultrathin ZSM-5 zeolite nanosheet laminated membrane for high-flux desalination of concentrated brines. *Sci. Adv.* **4**, eaau8634 (2018).
22. D. Kim, M. Shete, M. Tsapatsis, Large-grain, oriented, and thin zeolite MFI films from directly synthesized nanosheet coatings. *Chem. Mater.* **30**, 3545–3551 (2018).
23. Y. Peng, X. Lu, Z. Wang, Y. Yan, Fabrication of b-oriented MFI zeolite films under neutral conditions without the use of hydrogen fluoride. *Angew. Chem. Int. Ed.* **54**, 5709–5712 (2015).
24. D. Fu, J. E. Schmidt, Z. Ristanović, A. D. Chowdhury, F. Meirer, B. M. Weckhuysen, Highly oriented growth of catalytically active zeolite ZSM-5 films with a broad range of Si/Al ratios. *Angew. Chem. Int. Ed.* **56**, 11217–11221 (2017).
25. A. Corma, V. Fornes, S. B. Pergher, T. L. M. Maesen, J. G. Buglass, Delaminated zeolite precursors as selective acidic catalysts. *Nature* **396**, 353–356 (1998).
26. K. Varoon, X. Zhang, B. Elyassi, D. D. Brewer, M. Gettel, S. Kumar, J. A. Lee, S. Maheshwari, A. Mittal, C. Y. Sung, M. Cococcioni, L. F. Francis, A. V. McCormick, K. A. Mkhoyan, M. Tsapatsis, Dispersible exfoliated zeolite nanosheets and their application as a selective membrane. *Science* **334**, 72–75 (2011).
27. K. V. Agrawal, B. Topuz, T. C. T. Pham, T. H. Nguyen, N. Sauer, N. Rangnekar, H. Zhang, K. Narasimharao, S. N. Basahel, L. F. Francis, C. W. Macosko, S. Al-Thabaiti, M. Tsapatsis, K. B. Yoon, Oriented MFI membranes by gel-less secondary growth of sub-100 nm MFI-nanosheet seed layers. *Adv. Mater.* **27**, 3243–3249 (2015).
28. W. J. Roth, T. Sasaki, K. Wolski, Y. Song, D.-M. Tang, Y. Ebina, R. Ma, J. Grzybek, K. Kałahurska, B. Gil, M. Mazur, S. Zapotoczny, J. Cejka, Liquid dispersions of zeolite monolayers with high catalytic activity prepared by soft-chemical exfoliation. *Sci. Adv.* **6**, eaay8163 (2020).
29. S. Sabnis, V. A. Tanna, C. Li, J. Zhu, V. Vattipalli, S. S. Nonnenmann, G. Sheng, Z. Lai, H. H. Winter, W. Fan, Exfoliation of two-dimensional zeolites in liquid polybutadienes. *Chem. Commun.* **53**, 7011–7014 (2017).
30. M. Y. Jeon, D. Kim, P. Kumar, P. S. Lee, N. Rangnekar, P. Bai, M. Shete, B. Elyassi, H. S. Lee, K. Narasimharao, S. N. Basahel, S. Al-Thabaiti, W. Xu, H. J. Cho, E. O. Fetisov, R. Thyagarajan, R. F. DeJaco, W. Fan, K. A. Mkhoyan, J. I. Siepmann, M. Tsapatsis, Ultra-selective high-flux membranes from directly synthesized zeolite nanosheets. *Nature* **543**, 690–694 (2017).
31. Y. Liu, W. Qiang, T. Ji, M. Zhang, M. Li, J. Lu, Y. Liu, Uniform hierarchical MFI nanosheets prepared via anisotropic etching for solution-based sub–100-nm-thick oriented MFI layer fabrication. *Sci. Adv.* **6**, eaay5993 (2020).
32. W. Chaikittisilp, Y. Suzuki, R. R. Mukti, T. Suzuki, K. Sugita, K. Itabashi, A. Shimojima, T. Okubo, Formation of hierarchically organized zeolites by sequential intergrowth. *Angew. Chem. Int. Ed.* **52**, 3355–3359 (2013).
33. M. Shete, M. Kumar, D. Kim, N. Rangnekar, D. Xu, B. Topuz, K. V. Agrawal, E. Karapetrova, B. Stottrup, S. Al-Thabaiti, S. Basahel, K. Narasimharao, J. D. Rimer, M. Tsapatsis, Nanoscale control of homoepitaxial growth on a two-dimensional zeolite. *Angew. Chem. Int. Ed.* **56**, 535–539 (2017).

34. X. Zhang, D. Liu, D. Xu, S. Asahina, K. A. Cychosz, K. V. Agrawal, Y. Al Wahedi, A. Bhan, S. Al Hashimi, O. Terasaki, M. Thommes, M. Tsapatsis, Synthesis of self-pillared zeolite nanosheets by repetitive branching. *Science* **336**, 1684–1687 (2012).
35. P. Kumar, D. W. Kim, N. Rangnekar, H. Xu, E. O. Fetisov, S. Ghosh, H. Zhang, Q. Xiao, M. Shete, J. I. Siepmann, T. Dumitrica, B. McCool, M. Tsapatsis, K. A. Mkhoyan, One-dimensional intergrowths in two-dimensional zeolite nanosheets and their effect on ultra-selective transport. *Nat. Mater.* **19**, 443–449 (2020).
36. D. Kim, M. Y. Jeon, B. L. Stottrup, M. Tsapatsis, Para-Xylene ultra-selective zeolite MFI membranes fabricated from nanosheet monolayers at the air-water interface. *Angew. Chem. Int. Ed.* **57**, 480–485 (2018).
37. J. D. Kestell, K. Mudiyanselage, X. Ye, C.-Y. Nam, D. Stacchiola, J. Sadowski, J. A. Boscoboinik, Stand-alone polarization-modulation infrared reflection absorption spectroscopy instrument optimized for the study of catalytic processes at elevated pressures. *Rev. Sci. Instrum.* **88**, 105109 (2017).
38. C. N. Eads, J.-Q. Zhong, D. Kim, N. Akter, Z. Chen, A. M. Norton, V. Lee, J. A. Kelber, M. Tsapatsis, J. A. Boscoboinik, J. T. Sadowski, P. Zahl, X. Tong, D. J. Stacchiola, A. R. Head, S. A. Tenney, Multi-modal surface analysis of porous films under *operando* conditions. *AIP Adv.* **10**, 085109 (2020).
39. J. D. Kestell, J. Zhong, M. Shete, I. Waluyo, J. T. Sadowski, D. J. Stacchiola, M. Tsapatsis, J. A. Boscoboinik, Studying two-dimensional zeolites with the tools of surface science: MFI nanosheets on Au(111). *Catal. Today* **280**, 283–288 (2017).
40. Y. Ma, M. L. Jue, F. Zhang, R. Mathias, H. Y. Jang, R. P. Lively, Creation of well-defined "mid-sized" micropores in carbon molecular sieve membranes. *Angew. Chem. Int. Ed.* **58**, 13259–13265 (2019).
41. W. Yuan, Y. S. Lin, W. Yang, Molecular sieving MFI-type zeolite membranes for pervaporation separation of xylene isomers. *J. Am. Chem. Soc.* **126**, 4776–4777 (2004).
42. X. Wu, W. Wei, J. Jiang, J. Caro, A. Huang, High-flux high-selectivity metal–organic framework MIL-160 membrane for xylene isomer separation by pervaporation. *Angew. Chem. Int. Ed.* **57**, 15354–15358 (2018).
43. D.-Y. Koh, B. A. McCool, H. W. Deckman, R. P. Lively, Reverse osmosis molecular differentiation of organic liquids using carbon molecular sieve membranes. *Science* **353**, 804–807 (2016).
44. M. Tsapatsis, G. R. Gavalas, Synthesis of porous inorganic membranes. *MRS Bull.* **24**, 30–35 (1999).
45. C. D. Baertsch, H. H. Funke, J. L. Falconer, R. D. Noble, Permeation of aromatic hydrocarbon vapors through silicalite-zeolite membranes. *J. Phys. Chem.* **100**, 7676–7679 (1996).
46. G. Xomeritakis, S. Nair, M. Tsapatsis, Transport properties of alumina-supported MFI membranes made by secondary (seeded) growth. *Microporous Mesoporous Mater.* **38**, 61–73 (2000).
47. W. Chaikittisilp, M. E. Davis, T. Okubo, TPA^+-mediated conversion of silicon wafer into preferentially-oriented MFI zeolite film under steaming. *Chem. Mater.* **19**, 4120–4122 (2007).
48. S. Aguado, E. E. McLeary, A. Nijmeijer, M. Luiten, J. C. Jansen, F. Kapteijn, b-Oriented MFI membranes prepared from porous silica coatings. *Microporous Mesoporous Mater.* **120**, 165–169 (2009).
49. P. Karakiliç, R. Toyoda, F. Kapteijn, A. Nijmeijer, L. Winnubst, From amorphous to crystalline: Transformation of silica membranes into silicalite-1 (MFI) zeolite layers. *Microporous Mesoporous Mater.* **276**, 52–61 (2019).
50. D. Zhao, P. Yang, N. Melosh, J. Feng, B. F. Chmelka, G. D. Stucky, Continuous mesoporous silica films with highly ordered large pore structures. *Adv. Mater.* **10**, 1380–1385 (1998).
51. D. Kim, B. F. Chmelka, Robust transparent mesoporous silica membranes as matrices for colorimetric sensors. *RSC Adv.* **5**, 16549–16553 (2015).
52. T. C. T. Pham, T. H. Nguyen, K. B. Yoon, Gel-free secondary growth of uniformly oriented silica MFI zeolite films and application for xylene separation. *Angew. Chem. Int. Ed.* **52**, 8693–8698 (2013).
53. K. S. Pitzer, D. W. Scott, The thermodynamics and molecular structure of benzene and its methyl Derivatives. *J. Am. Chem. Soc.* **65**, 803–829 (1943).
54. C. B. Willingham, W. J. Taylor, J. M. Pignocco, F. D. Rossini, Vapor pressures and boiling points of some paraffin, alkylcyclopentane, alkylcyclohexane, and alkylbenzene hydrocarbons. *J. Res. Natl. Bur. Stand.* **35**, 219–244 (1945).
55. L. Zhang, L. L. Li, N. J. Liu, H. L. Chen, Z. R. Pan, S. J. Lue, Pervaporation behavior of PVA membrane containing β-cyclodextrin for separating xylene isomeric mixtures. *AIChE J.* **59**, 604–612 (2013).
56. X. Y. Qu, H. Dong, Z. J. Zhou, L. Zhang, H. L. Chen, Pervaporation separation of xylene isomers by hybrid membranes of PAAS filled with silane-modified zeolite. *Ind. Eng. Chem. Res.* **49**, 7504–7514 (2010).

Acknowledgments: S.G. and K.A.M. would like to acknowledge P. Kumar for discussions. **Funding:** We extend our appreciation to the Deputyship for Research and Innovation, Ministry of Education in Saudi Arabia for funding aspects of this research work through the project number (721). Membrane synthesis and permeation measurements are based upon work supported by the U.S. Department of Energy's Office of Energy Efficiency and Renewable Energy (EERE) under the Advanced Manufacturing Office Award Number DE-EE0007888. Support for the fabrication of porous supports was provided by a National Research Foundation of Korea (NRF) grant funded by the Korean government (MSIT) (no. 2021R1A2C1095078). S.G. and K.A.M. were supported by the NSF through the University of Minnesota MRSEC under award number DMR-2011401. A.K. acknowledges support from the National Science Foundation Graduate Research Fellowship Program under grant no. (DGE-1746891). Parts of this work were carried out in the Characterization Facility, University of Minnesota, which receives partial support from the NSF through the MRSEC (DMR-2011401). PM-IRRAS experiments were performed at the Center for Functional Nanomaterials, Brookhaven National Laboratory, supported by the U.S. Department of Energy, Office of Basic Energy Sciences, under contract no. DE-SC0012704. In-plane grazing incidence synchrotron XRD data were collected on beamline 33-BM-C at the Advanced Photon Source, Argonne National Laboratory supported by the U.S. Department of Energy, Office of Science, Office of Basic Energy Sciences, under contract no. DE-AC02-06CH11357. **Author contributions:** M.T. directed the project. D.K. and M.T. conceived the work, and D.K. synthesized the nanosheets. D.K., S.G., and A.K. performed characterization of the nanosheets, and with K.A.M. and M.T. analyzed the results. D.K., N.A., and J.A.B. performed PM-IRRAS measurements. D.K. and G.G. fabricated the membranes, and with X.D. characterized the membranes. D.K., N.R., J.R.J., K.N., M.A.M., S.A.-T., and B.M. performed and/or analyzed the permeation tests. D.K., S.G., A.K., and M.T. wrote the manuscript with written contributions from all authors. **Competing interests:** The authors declare that they have no competing interests. **Data and materials availability:** All data needed to evaluate the conclusions in the paper are present in the paper and/or the Supplementary Materials.

Submitted 14 October 2021
Accepted 11 February 2022
Published 6 April 2022
10.1126/sciadv.abm8162